Vibronic Motion with Joint Angstrom–Femtosecond Resolution Observed through Fano Progressions Recorded within One Molecule

Joonhee Lee, Shawn M. Perdue, Alejandro Rodriguez Perez, and Vartkess Ara Apkarian*

Department of Chemistry, University of California, Irvine, California 92697-2025, United States

ABSTRACT Electroluminescence (EL) in scanning tunneling microscopy (STM), which enables spectroscopy with submolecular spatial resolution, is shown to be due to radiative ionization with vibronic shape resonances that carry Fano line profiles. Since Fano progressions retain phase information, the spectra can be transformed to the time domain to reconstruct the vibronic motion. In effect, measurements within a molecule are accessible with joint space–time resolution at the Å–fs limit. We demonstrate this through EL-STM on the Jahn–Teller-active Zn-etioporphyrin radical anion and visualize the orbiting motion of scattered electrons upon sudden reduction and oxidation. We discuss the elements that enable spectroscopy with submolecular spatial resolution through EL-STM and the closely related STM-Raman process.

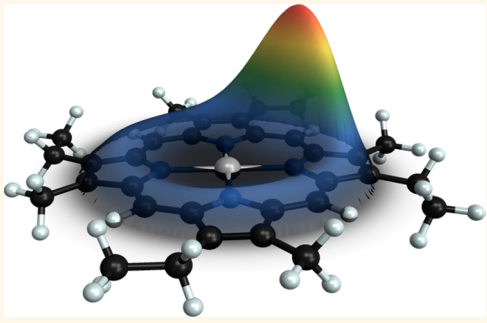

KEYWORDS: scanning tunneling microscopy · submolecular spectroscopy · Jahn–Teller effect · electroluminescence · Fano line shape

Molecular spectroscopy with submolecular spatial resolution has been realized in two closely related methods using a scanning tunneling microscope (STM). Ho *et al.* demonstrated that electroluminescence (EL) induced by tunneling electrons yields vibronic spectra that depend on placement of the STM tip within a molecule, on single molecules of Zn-etioporphyrin (ZnEtio) and Mg-porphyrin (MgP).[1,2] More recently, Raman spectroscopy (RS) driven by the STM junction plasmon (STM-RS) was demonstrated with submolecular spatial resolution on *meso*-tetrakis-(3,5-ditertiarybutylphenyl)porphyrin (H_2TBPP).[3] This variant of tip-enhanced Raman (TERS) builds upon prior linear[4] and nonlinear[5] EL-STM measurements on porphyrin multilayers by the same group. Rather than TERS driven by plasmon fields,[6,7] the spatial resolution of which is determined by field decay lengths of >10 nm, the realized Å-scale resolution in STM-RS indicates plasmon-driven injection of tunneling electrons, as in charge transfer plasmon Raman (CTPR) recently identified at the fusing junction of a nanodumbbell.[8] The demonstrated spatial resolution in these mixed photo-electrospectroscopic methods circumvents diffraction considerations that limit nonlinear optical microscopy. While aspects of EL-STM have been addressed through theory,[9,10] mechanistic details are not understood in sufficient clarity to generalize principles. Here, we reinvestigate EL-STM on ZnEtio to clarify the operating mechanism based on our recent STM investigation of the same system.[11]

ZnEtio adsorbs in its reduced form on metal surfaces and readily charges on insulating films, and the topographic images of $ZnEtio^-$ can be quantitatively understood as that of a Jahn–Teller (JT)-active radical anion in which the unpaired π-electron is delocalized over the macrocycle.[11] It is easily verified that the vibronic EL spectra arise upon injecting a tunneling electron in the anion, and the luminescence can be directly assigned to radiative ionization of the $ZnEtio^=$ dianion. In addition to providing a consistent interpretation of optical and tunneling spectra, this assignment explains the key consideration for radiative transitions

* Address correspondence to aapkaria@uci.edu.

Received for review October 13, 2013 and accepted November 21, 2013.

Published online November 22, 2013
10.1021/nn405335h

to compete with fast (>10^{14} s^{-1}) tunneling rates because it offers a large transition dipole along the tip *z*-axis which can be enhanced by the junction plasmon. Field enhancement is an essential ingredient in radiative inelastic scattering of tunneling electrons, which is widely seen in STM on clean metal surfaces,[12] surfaces decorated with metal clusters or atoms,[13] clusters on oxide films,[14] on molecular multilayers, and on single molecules that are decoupled from the metal substrate by an insulating thin film.[15,16] Invariably, the transitions must couple to radiative modes of the junction plasmon.[17−19] While the *z*-projection of transition dipoles is enhanced, components parallel to the substrate are quenched.[20] Remarkably, the accounts of spectroscopy with submolecular spatial resolution are on planar porphyrins, the optical spectra of which arise from in-plane $\pi-\pi^*$ transitions.[21] Rather than charge preserving electronic excitation by electron−hole injection, as previously offered and modeled,[2,9,10] transitions perpendicular to the molecular plane are required to rationalize plasmon-enhanced luminescence of porphyrins. This is provided in reductive or oxidative scattering channels that do not conserve molecular charge. The same consideration would suggest that STM-RS arises from plasmon-coupled electron transfer between tip and molecule. This mechanism provides the requisite *z*-dipole along with the requirement of wave function overlap for photoinduced charge transfer between tip and molecule, which is essential to explain the spatial resolution seen in STM-RS. These general considerations are put on a firmer footing with the detailed analysis of EL-STM that we provide.

Given an understanding of operating mechanisms, it is valuable to recognize the novelty of information in submolecular spectroscopy. We will show that vibronic structure in radiative ionization arises from shape resonances over the ionization continuum. In direct analogy with Fano's original analysis of autoionizing spectra, the interference between discrete resonances and continuum leads to dispersive line shapes.[22,23] We recognize that Fano progressions retain phase information, and as such, the spectra can be transformed to the time domain. We present a general formulation of the Fano profile in conjugate time-frequency representation and extend the idealization of the original from a white continuum to a more realistic background. We implement the spectral analysis to underscore that, under considerations that are not too restrictive, EL-STM gives access to inner workings of a molecule with joint Å−fs resolution. This is illustrated by visualizing the motion of the JT-active electron upon sudden reduction−oxidation of the radical anion, that is, formation of the $ZnEtio^{=}$ and its rapid radiative ionization back to $ZnEtio^{-}$. A rather simple motion is captured by the shape resonances, despite the nontrivial underlying multidimensional JT Hamiltonian in $E\otimes(b_1\oplus b_2)$ symmetry.[24]

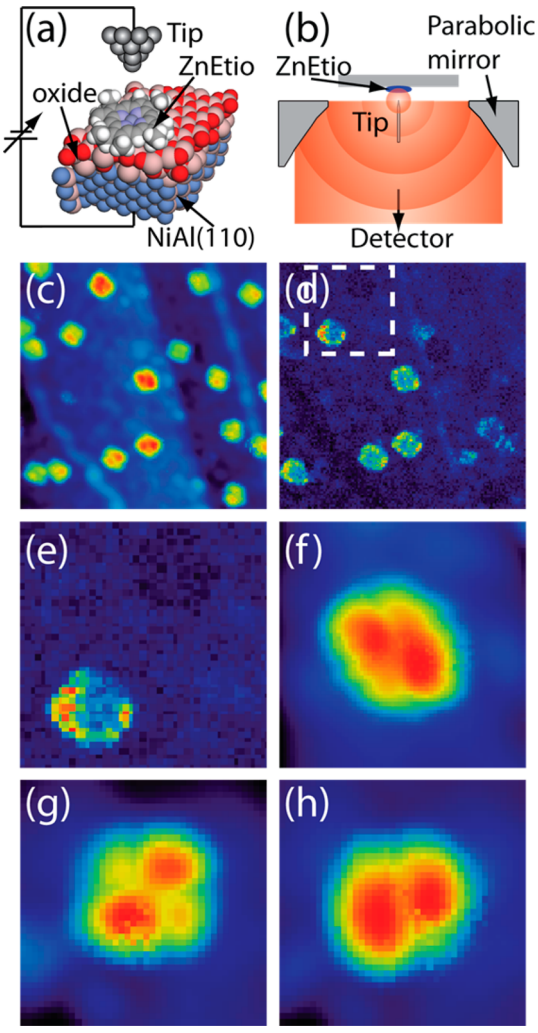

Figure 1. Simultaneously recorded topographic and EL images of $ZnEtio^{-}$. (a) Experimental setup illustrating a $ZnEtio^{-}$ adsorbed on the oxide film grown on NiAl(110) surface.[11] (b) Photon collection setup used for recording EL images. (c) Topography. (d) EL image simultaneously taken with the topography (c) using an avalanche photodiode (APD) with 1 s integration time. (e) Magnified image of the dashed box in (d) showing negative contrast. (f) Close-up of a saddle molecule at the center of image (c). (g) Topography of luminescing saddle molecule. (h) Same molecule (g) no longer showing EL after going through a conformational change.

In what follows, we present the essential experimental measurements for mechanistic interpretations of EL-STM on $ZnEtio^{-}$. The spatially resolved spectra are assigned based on symmetry considerations, and vibronic progressions are analyzed as shape resonances. We then present the formulation of the Fano line profile, which we use for quantitative analysis of the spectra. This allows transformation of the spatially resolved spectra from space−frequency to space−time, to reconstruct motion inside a single molecule.

RESULTS AND DISCUSSION

In Figure 1c,d, we show simultaneously recorded STM and EL images of single molecules on the oxide. On the oxide, ZnEtio shows a hysteretic scanning

tunneling spectrum (STS) characteristic of charging and discharging. The molecule charges at $V_b \sim 0.7$ eV and remains negatively charged until the bias is lowered below $V_b \sim -0.5$ V.[11] The images in Figure 1, which are recorded at $V_b = 2.2$ V, belong to ZnEtio$^-$. Significant variation in both images can be seen—only a subset of the molecules luminesce on the nominally weakly interacting substrate. Close-ups of emitting and non-emitting molecules are shown in Figure 1e,f. The EL image of the dark molecule shows negative contrast (Figure 1e) due to effective blocking of the EL background of the oxide. Evidently, the dark molecule provides an efficient nonradiative inelastic electron scattering channel. The topography of the luminescing molecules is invariably the "saddle"-shaped (Figure 1f,g). The apparent shape, a quadrupolar dimple with uneven lobes, can be reproduced as the density of a JT electron delocalized on a disk, coupled to deformations of the disk.[11] We will refer to the orthogonal pair of lobes as big lobe (BL) and small lobe (SL) for obvious reasons. Some luminescing molecules switch off after extended periods of measurement, with concomitant change in their apparent shape. The topographic images in Figure 1g,h are from such a molecule. The sensitivity in apparent shape of a molecule to small variations in local structure of the substrate is a hallmark of JT instability, as demonstrated by reproducing observed distortions with the inclusion of small crystal fields in the JT potential.[11] However, the atomistic nature of the local structural variations is not clear at present. In contrast, DFT calculations of neutral molecules on the oxide indicate that the density of states of ZnEtio molecules is insensitive to adsorption sites due to the weak van der Waals binding.[25]

The characteristic STS (d*I*/d*V* *vs* V_b) of luminescing molecules is shown in Figure 2. It shows a pair of bands that straddle the Fermi energy: a sharp resonance at 0.4 V and its broader counterpart at −0.5 eV. This motif fits the model of bipolar conductivity through a filled orbital in a double barrier junction.[26] However, a more consistent interpretation of all observations is obtained by assigning the sharp and broad peaks to the singly unoccupied (SUMO) and singly occupied (SOMO) spin orbitals of the anion.[11] The injection of an electron into the SUMO prepares the transient dianion [A$^- + e^-$], which is unstable below ~2 eV, namely, the energy difference between optimized structures of ZnEtio$^-$ and ZnEtio$^=$. Since the injection of an electron on an already negative ion is subject to Coulomb blockade,[27] the splitting between spin-orbitals can be equated to the Coulomb charging energy $e^2/R \sim 1$ eV to extract a separation $R = 14$ Å between the electrons, which is consistent with them being on opposite sides of the disk. The width of the sharp resonance yields a lifetime $\tau = \hbar/2\Delta E = 35$ fs for the transient state. A scattering state in which a weakly interacting electron scatters on the strongly bound electron of the anion [A$^- + e^-$] can be recognized as a shape resonance,

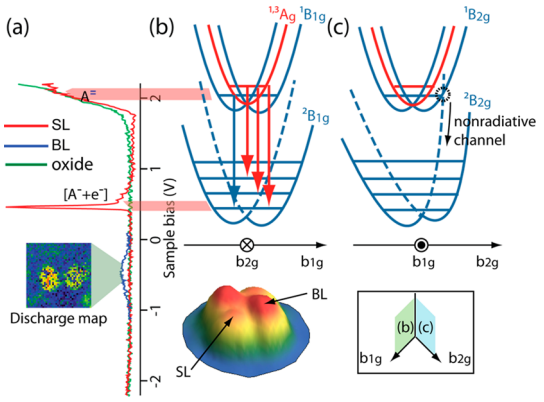

Figure 2. d*I*/d*V* spectra of a luminescing molecule and the associated potential energy surfaces. (a) d*I*/d*V* spectra from a SL, BL of ZnEtio$^-$, and the oxide film.[11] (b) Two-dimensional representation of JT potential surfaces along the B_{1g} coordinate (blue) associated with the d*I*/d*V* curve and optical transitions. The dashed lines indicate the conical intersection. The JT potential in the excited state quenches and a new potential (red) along totally symmetric modes arises upon electron injection to SL. The saddle topography is illustrated below the ground state potential surface, indicating that the saddle shape arises from the JT potential wells formed along b_{1g} distortion. (c) JT potential surfaces along b_{2g} coordinate showing the curve crossing leading to a nonradiative channel. The inset shows the vibrational coordinate space in 3D.

familiar in atom and molecule scattering[28,29] and seen in electron energy loss spectra of adsorbates.[30] Consistent with the picture of a discrete scattering state embedded in a conduction continuum, the line shape of the sharp resonance is dispersive and can be fit to the modified Fano profile of single channel 1D conductivity.[31−34] For scattering on a JT-active anion, vibronic channels open up, which explains the vibronic tunneling spectra previously seen on the SUMO.[35]

The broad band of the STS at 2 V, which is common to spectra recorded on the molecule and on the oxide (off the molecule), is dominated by the opening of the conduction band of the aluminum oxide.[36] EL with a sharp energy threshold is observed upon accessing the 2 eV band, as illustrated in the bias-dependent spectra recorded on the BL and SL, which are shown in Figure 3a,b. On the BLs, a single dark Fano line is seen (at 1.68 eV) over the continuum. On the SL, a vibronic progression with origin at 1.74 eV is seen over the same continuum. While the blue edge of the continuum shifts with bias, the line positions do not, indicating that the line spectra are due to vibrationally relaxed emission. The excitation threshold of 2 V places the terminal state of the vibronic progression on the sharp STS resonance at 0.4 V, as indicated in Figure 2. Given the identification of the terminal state as the transient dianion, [A$^- + e^-$], the vibrationally relaxed emitting states can be recognized as the bound electronic states of the dianion, A$^=$ (Figure 2a). The spatial maps of the spectral features in Figure 3c are shown in Figure 3d−f. In all maps, the center of the molecule is silent, clarifying that the transitions are limited to the π-electrons.

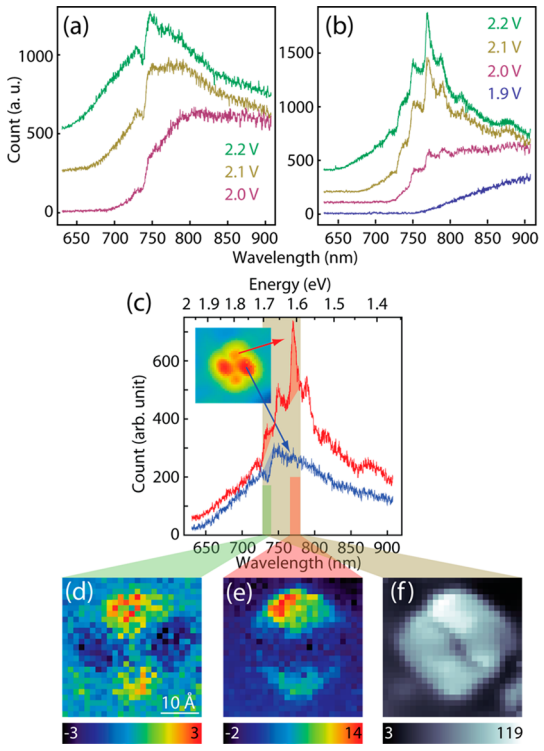

Figure 3. EL spectral mapping inside a single molecule. Bias dependence of spectra on BL (a) and SL (b). Two characteristic single point spectra recorded within the molecule in the inset (c), and spectral maps generated by integration of the emission intensity over the indicated bands: integration of the background-subtracted shaded areas between 727 and 741 nm (d) and 763−784 nm band (e), total intensity over the 727−784 nm band (f). The unit of integrated intensity is 1000 CCD counts. The maps are generated from spectra recorded on each pixel of a 25 × 25 grid, with 1 min integration time per spectrum, at 0.1 nA, 2.2 V. The total acquisition time to complete the mapping is 11 h.

The signed map of Figure 3d shows the two emitting states that lead to the progression and the single line to be spatially orthogonal. The map in Figure 3d is for the integrated intensity over a narrow spectral band that encompasses the BL line and its neighboring SL line. It is signed because of the shift in vibronic origin of ~60 meV. A third, nonradiative upper state is evident by the nodal plane in the map of emission integrated over the 745−780 nm band (Figure 3f). Given the fourfold symmetry of the molecule, the absence of the mirror image of a nodal plane at +45° is remarkable. The broken symmetry of this map must arise from crystal field splitting. It arises naturally as an asymmetric curve crossing where the cone of the JT potential is tilted (Figure 2c).

Spectral Assignments. Symmetry considerations are sufficient to fully assign the spectra. The ZnEtio$^-$ radical anion is a classic example of the JT effect in $E\otimes(b_1\oplus b_2)$ symmetry. The odd electron occupies the doubly degenerate E_g orbital of the neutral form, which in D_{4h} symmetry stabilizes by coupling to rectangular (b_{1g}) and rhombic (b_{2g}) vibrational distortions that transform as x^2-y^2 and xy, respectively. Inspection of the topographic image of Figure 1 is sufficient to conclude that the vibronic ground state of the radical anion has $^2B_{1g}(x^2-y^2)$ overall symmetry. Its uneven lobes are a consequence of the crystal field of the oxide, which splits the potential minima along the vertical and horizontal rectangular distortions and tilts the cone of the adiabatic potential. The injection of a second electron in the degenerate E_g orbital gives rise to $E_g \otimes E_g = {}^1A_{1g} + {}^3A_{2g} + {}^1B_{1g} + {}^1B_{2g}$ electronic states of the dianion. Since totally symmetric A states are JT-inactive, their potential minima remain at the origin, and the relative displacement of potentials leads to Franck−Condon activity. As such, the progression observed on the SLs can be assigned to the $^{1,3}A_g \rightarrow {}^2B_{1g}$ transition (Figure 2b). The single line seen on the BLs implies a transition between vertically aligned potentials and, therefore, identifies the $^1B_{1g} \rightarrow {}^2B_{1g}$ transition. The nodal plane in the integrated emission (Figure 3f) occurs along the b_{2g} rhombic distortion and identifies the nonradiative channel as the crossing between the tilted cone and the B_{2g} electronic state. Thus, the spatial maps allow a complete accounting of the bound two-electron states that are prepared, and an important propensity rule emerges: injection of an electron on the BLs leads to JT-active states of double occupancy, e_g^2, while injection in the SLs leads to JT-inactive states of single occupancy, $e_g^1e_g^1$. The system behaves as if the odd electron of the anion is in the BL, as in the discharge map of the anion (Figure 2a).[11]

In summary, spatial maps of the resolved vibronic emission can be fully understood as transitions from the bound states of the ZnEtio$^=$ that terminate on the JT-active ZnEtio$^-$ with the release of an electron. The same conclusion would be reached based on the observed energetics. With ZnEtio$^=$ prepared at $V_b = 2$ eV, the radiation at $\hbar\omega = 1.6$ eV probes the same vibronic shape resonances as the STS at 0.4 eV. Consistent with this assignment, both STS and vibronic lines exhibit Fano profiles. The interference between two radiative channels that generates the Fano line shape implies a continuum of direct radiative ionization on the repulsive Coulombic potential of the dianion:[37,38]

$$A^= \rightarrow A^- + \hbar\omega + e^- \qquad (1)$$

and a progression of autoionizing shape resonances, bound inside the Coulomb repulsion shell,[37] in which the ionizing electron transiently orbits the anion before departing:

$$A^= \rightarrow [A^-(l, v) + e^-] + \hbar\omega \rightarrow A^- + e^- \qquad (2)$$

The direct analogy of this scheme with the original Fano problem should not be lost. Fano's analysis was for autoionizing two-electron resonances in helium.[23] Here, the upper state of the dianion is bound, while the lower energy terminal state consists of scattering states. This unusual inversion in energy between bound and scattering states occurs for two electrons confined to a ring.[39] As such, the autoionization resonances appear in

emission. The spectra can be perfectly fitted in this context, as shown in Figure 4a,b. Below, we will expand on the fitting procedure and the information content that can be extracted. Here, we point out that fitting is essential to extract accurate line positions for dispersive lines, and we note the striking simplicity of the vibronic spectra—a single resonance on the BLs and a single progression with a pronounced negative anharmonicity on the SLs.

Orbiting Resonances. The orbiting resonances in eq 2 couple to the internal vibronic excitations (l,v) of the JT-active anion, consisting of the orbital angular momentum of the electron, l, and the vibrational excitation, v, of the skeletal deformation. As such, the level structure must simultaneously reflect both motions. The formally $E\otimes(b_1\oplus b_2)$ problem, to which the system belongs, does not have a trivial solution.[40] This is further complicated by the fact that in ZnEtio$^-$ there are nine normal modes each of b_1 and b_2 symmetry.[41] The multimode JT dynamics is usually reduced to a single effective deformation; however, even in idealized cases, an irregular density of states arises.[42] Even when one vibration of each symmetry is involved, where frequencies and couplings are different, chaotic trajectories emerge in the vibronic dynamics.[43] Two limiting cases allow simple solutions: in the case of accidental degeneracy, $\omega(b_1) \sim \omega(b_2)$, the problem reduces to $E\otimes e$, with known general algebraic solutions,[44,45] and in the limit where coupling to one of the modes can be ignored, the problem reduces to 1D with trivial vibrational level structure.[46] The initial constant level spacing seen in Figure 2b would suggest that a harmonic frequency of ω = 320 cm^{-1} and a displacement of 0.3 Å between the $A^{=}(A_{1g})$ and $A^{-}(B_{1g})$ potentials can be extracted from the Franck–Condon factors. However, the 1D case cannot account for the negative anharmonicity seen in Figure 4c; moreover, there is no basis for singling out a dominant mode among the JT-active vibrations, and in the absence of pseudorotation, orbiting electron resonances cannot be sustained. Quasiperiodic orbits arise when JT stabilization energies along the two coordinates are similar, $E^1_{JT} \sim E^2_{JT}$, where $E^i_{JT} = c_i^2/2K_i$ is the ratio between vibronic coupling and force constant. Our analysis of the ground state of the molecule shows that $\omega(b_1)/\omega(b_2) \sim 1.04$.[11] Accordingly, we assign the progression to the same effective deformation and recognize that the observed level structure perfectly fits the orbiting states of an electron confined to a disk. Thus, assuming a potential $V = 0$ for $r < R$ and $V = \infty$ for $r > R$, the wave functions are the cylindrical Bessel functions with first root limited to the radius of the disk R.[11] The states and energy levels are given as

$$\psi_{\ell}(r,\vartheta) = NJ_{\ell}(k_{\ell}r)e^{i\ell\vartheta};\ E_{\ell} = \hbar^2\alpha_{\ell}^2/2m^*R^2;\ \text{and}$$
$$\ell = \pm\frac{1}{2}, \pm\frac{3}{2}\ldots \qquad (3)$$

where $k_{\ell}R$ is the first root of the ℓth Bessel function (α_{ℓ} = 3.14, 4.49, 5.76,... for $\ell = -1/2, 3/2, 5/2,...$). The half-integer

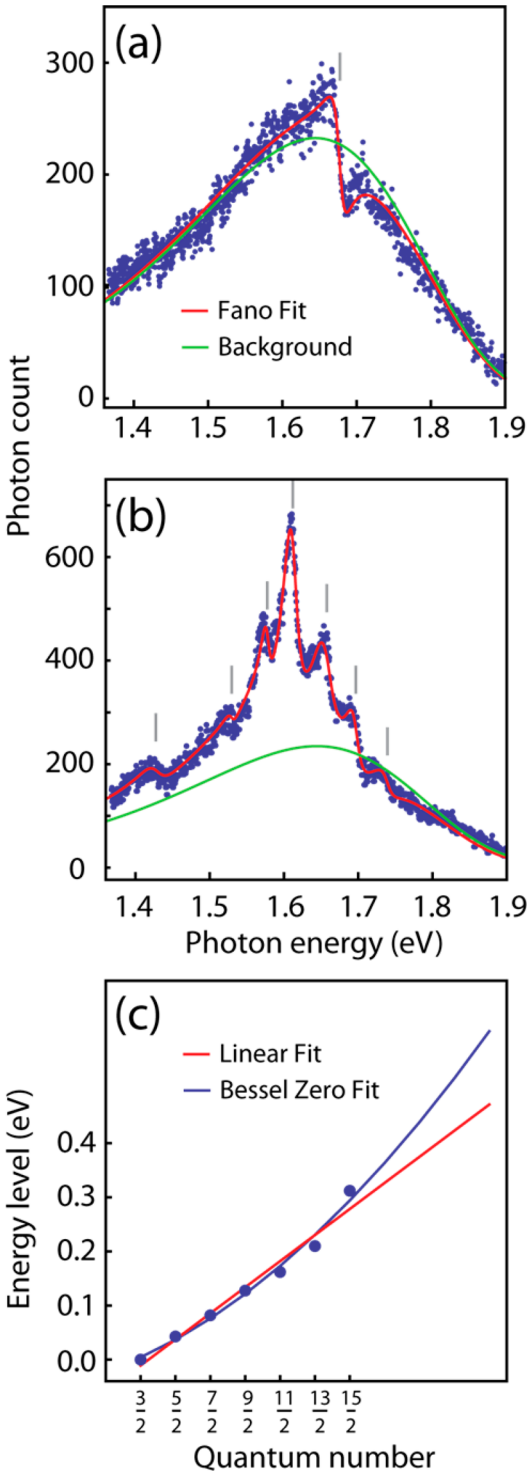

Figure 4. Fano fit to EL spectra. (a) Experimental spectrum on a BL (blue dots) and fit to Fano line shape (red curve) with background (green curve) due to the bound-free scattering continuum. Line positions are indicated by the gray bars. (b) Fit to the Fano progression on the SL (red) uses the background extracted from the BL (green). (c) Energy levels of progression (blue circles) extracted from the Fano fit in (b). Rather than a vibrational progression, which would show a constant level spacing (red line), the observed energy levels fit that of an orbiting electron confined to the disk (eq 3), shown with the continuous blue curve. The state numbering is obtained by matching the same curve to the pseudorotation states of the deformation.

angular momenta satisfy the Berry phase requirement, the radial functions avoid the origin, and the motion is on a Mobius strip.[47] The fit to the data is shown in Figure 4c. As would be expected for rotational motion, the energy levels E_{ℓ} are in quadratic form (eq 3); however, the decreasing separation between the Bessel roots for small ℓ yields a nearly constant initial level spacing ($E_{\ell} \propto \ell$, as $\ell \rightarrow 0$). For large ℓ, the level spacing becomes linear in ℓ ($E_{\ell} \propto \ell^2$). This level structure is the result of confinement on the disk. Assuming $R = 7$ Å, as obtained from the Coulomb charging energy of the transient two-electron state, an effective electron mass of $m^* = 28\ m_e$ is obtained from eq 3. The effective mass indicates that the electron is dragged by the vibrational pseudorotation, with energies $E_{\ell} = \hbar^2\ell(\ell+1)/2\mu q_0^2$ given by the reduced mass μ of the vibrational mode and displacement q_0 of the potential minimum.[48] Using $q_0 = 0.3$ Å, obtained from the FC factors, an excellent fit to the data can be obtained for a reduced mass of $\mu = 4.4$ amu and assuming that the first observed state of the progression is the $\ell = 3/2$ state. The extracted reduced mass is consistent with vibrations dominated by C−C stretches, in which case $\mu = 6$ amu would be expected. Thus, the observed progression can be rationalized in the JT picture of an orbital dragged by the pseudorotation of the skeletal deformation.

Radiation Rates. Beside the consistent interpretation of EL and STS spectra, radiative ionization accounts for transition rates and dipoles that enable EL-STM. Emission from π-electronic states involves the ejection of an initial p_z-electron into an outgoing wave with k_z-momentum. The associated transition dipole, $\mu_z \propto \int P(k_z)\langle k_z|\partial/\partial_z|p_z\rangle dk_z$ where $P(k_z)$ is the density of the momentum states sustained on the repulsive Coulomb potential (see below), is along the required direction to couple to the radiating modes of the junction plasmon. Moderate enhancements are sufficient for the emission to be observable. Since radiative ionization involves detachment of a full electron, the oscillator strength is near unity, $f \sim 1$, with spontaneous radiation rate of $\gamma_r = 8\pi^2e^2f/mc\lambda^2 \approx 10^9\ s^{-1}$. Assuming tunneling rates on the order of $\gamma_T \sim 10^{15}\ s^{-1}$, in the absence of enhancement, the quantum yield of emission cannot exceed $\phi = \gamma_r/(\gamma_r + \gamma_T) \sim 10^{-6}$. The acceleration of spontaneous emission by the local field of the plasmon, $\Gamma_r = \gamma_r|E_z/E_0|^2$,[20] for an electrochemically etched silver tip of 30 nm cone radius would predict a typical enhancement of $|E_z/E_0|^2 \sim 10^4$. A quantum yield of emission as high as 10^{-2} would be expected for electrons that scatter on the molecule. Correcting for direct tunneling into the oxide, the estimated net yields of 10^{-3}−10^{-5} agree with the experiment. A molecular π−π^* transition is simply incompatible with the observation of EL on porphyrins. Rather than enhancement, since $|E_{xy}/E_0| < 1$, emission perpendicular to the z-axis is quenched. Moreover, since radiation rates in the visible (Q-bands) are $\gamma_r < 10^7\ s^{-1}$, such emission from the molecular transitions would be 6−7 orders of magnitude less probable than radiative ionization. Finally, we note that, in the state assignments above, all identified one- and two-electron vibronic states are in the $E_g \otimes E_g$ space; therefore, all have even (g) symmetry with strictly forbidden dipole transitions among them. In radiative ionization (eq 2), the departing electron carries the transition dipole.

The same considerations apply to STM-RS. Raman is a luminescence process: absorption followed by spontaneous emission, with emission limited to the electronic coherence window. The principle distinction between STM-RS and EL-STM is the excitation mechanism. Instead of injecting an electron through the junction bias, in STM-RS, an electron must be photoinjected. Photoinjection of electrons in porphyrins has been demonstrated previously to be a rather inefficient process.[49] Once again, both excitation and emission processes must be enhanced by the junction plasmon; therefore, the transition dipole in both cases must lie along the tip z-axis. The rather natural assignment would be for a tip s-electron to be photoinjected into the porphyrin p_z orbital, $\langle\mu\rangle = \langle s|\mu|p_z\rangle$, in what may be regarded as an intermolecular charge transfer transition. Since the Raman scattering intensity is given by the polarizability $\alpha = |\langle g|\mu|e\rangle\langle e|\mu|g\rangle| = e^2|\langle s|z|p_z\rangle|^2$. The spatial dependence of STM-RS is closely related to the exponential distance dependence of STM given by the overlap between tip and molecule wave functions, $|\langle s|p_z\rangle|^2$.[50] Note, the vibrations seen in resonant Raman (RR) would include all JT-active modes. Thus, considering RR in its more natural time domain representation, the intensities of various vibrational modes can be obtained as their overlap $I_v \propto |\langle\psi_v|R\rangle|^2$ with the Raman $|R\rangle$ packet which develops in time:[51]

$$|R\rangle = \int_0^{\infty} e^{-iH_e t/\hbar}\mu|\psi_0\rangle dt \qquad (4)$$

in which $H_e = T_e + V_e$ is the excited state Hamiltonian. For the short time evolution of relevance, the excited state charge transfer potential (anion along the molecular coordinates) may be expanded at the ground state configuration:

$$V_e(q_i) = V_0 + \sum_i \left(\frac{\partial V}{\partial q_i}\right)_0 q_i \qquad (5)$$

The instantaneous forces along the various coordinates dictate the inertial motion of the Raman packet and the multidimensional evolution limits RR to fundamental transitions, $v = 1 \rightarrow v = 0$.[52] The observable modes will be those that are shifted by the photoreduction, and this includes the JT-active modes.

Fano Line Profiles in Time and Frequency Domains. Fano line profiles arise quite generally as the interference between continuum and discrete states, and extensive applications and interpretations exist in the literature. Rather than individual line profiles, our interest is in the unique information content in Fano progressions. Here

we show that given a physically motivated treatment of the continuum, the dispersive lines preserve full phase information and, therefore, retain complete knowledge of the underlying time domain dynamics. To see this, note that the Fano line shape function can be unsquared:

$$\frac{(q+\varepsilon)^2}{1+\varepsilon^2} = \left(\frac{q+\varepsilon}{1-i\varepsilon}\right)\left(\frac{q+\varepsilon}{1+i\varepsilon}\right) \equiv \mathscr{L}^*(\omega)\mathscr{L}(\omega) \quad (6)$$

in which q is the Fano coupling parameter and $\varepsilon = (\omega - \omega_0)/(\gamma/2)$ is the reduced frequency variable scaled by the width of the resonance, γ.[22] The inverse Fourier transform of $\mathscr{L}(\omega)$

$$\mathscr{F}_v^{-1}\left(\frac{q+\varepsilon}{1-i\varepsilon}\right) = (q-i)e^{-(i\omega_0+\frac{\gamma}{2})t} + i\delta(t) \quad (7)$$

makes it clear that it derives from the interference of a damped oscillator and a delta function in time, with complex amplitudes that determine the relative phase between them. It is instructive to consider the amplitude in polar form:

$$(q-i) = \csc(\phi)e^{-i\phi} \quad (8)$$

to note that the phase and amplitude of the transient state are related through the coupling parameter:

$$\phi = \arctan\left(\frac{1}{q}\right), \csc\phi = \sqrt{q^2+1} \quad (9)$$

In polar form, the spectral domain Fano profile reduces to

$$\frac{q+\varepsilon}{1-i\varepsilon} = \frac{\csc(\phi)e^{-i\phi}}{1-i\varepsilon} + i \quad (10)$$

The physical origin of the interference can be stated in time and frequency domain: The delta function in time (eq 7) provides for heterodyned detection of the evolution in the evanescent state at the discrete resonance $\omega = \omega_0$. In the spectral domain, the dispersive line arises from the cross term between the resonance and the flat background of unit intensity (eq 10). Thus, the continuum, which is quite generally colored, is idealized in Fano's treatment. Given a physically motivated spectral density for the continuum, $c(\omega)$, it can be substituted for the unit function in eq 10, with the rigor of the original treatment kept intact. This ensures a complete definition of the time domain evolution once the observed spectrum is reproduced. Equivalently, replacing $\delta(t)$ in eq 7 with a physically motivated time correlation function for the scattering states $c(t)$ would allow a parametric fit of the spectrum. Thus, for the continuum-corrected Fano profile, we define the Fourier pair:

$$\mathscr{L}_0(\omega) \equiv \frac{\csc(\phi)e^{-i\phi}}{1-\dfrac{i(\omega-\omega_0)}{\frac{\gamma}{2}}} + i\sqrt{c(\omega)} \Leftrightarrow \csc(\phi)e^{i\phi}e^{-(i\omega_0+\frac{\gamma}{2})t} + i\sqrt{c(t)} \equiv \mathscr{L}_0(t) \quad (11)$$

For an isolated line, this allows for background correction. If only a local fit is desired, then background functions with analytic transforms can be used. For example, since commonly $c(t)$ is a decaying function observed at early time, to ensure time reversibility, the inertial form may be adopted, $c(t) = \exp(-at^2 - bt)$, which in turn leads to the Voigt function for $c(\omega)$.

For progressions, the important quantity that is sought is the relative phases of the resonances to describe evolution of their superposition in time. As such, a global function of the background is required. With some generality, the functional form of the background is that of a bound-free transition:

$$c(t) = \langle\varphi(0)|\varphi(t)\rangle = \langle\varphi(0)|e^{-iHt}\varphi(0)\rangle \quad (12)$$

in which $\varphi(0)$ is the spatially localized initial bound state, and the evolution is on an unbound surface characterized by the potential $V(r)$ specific to a physical model. As in any time-dependent problem, it is more convenient to consider its spectral density. For bound-free transitions, analytic expressions can be obtained for $c(\omega)$ through the classical reflection approximation:[53]

$$c(\omega) = \int e^{j\omega t}c(t)dt \sim |V'(r(\omega))|^{-1}\varphi^2(r(\omega)) \quad (13)$$

in which $V(r)$ is the unbound potential. For radiative ionization, the scattering is onto a repulsive Coulomb shell on the terminal surface, $V(r) = E_0 + e^2/\varepsilon(r - r_0)$, and it is convenient to represent the localized initial state by a Gaussian $\varphi(0) = \exp(-r^2/d^2)$, to obtain

$$c(\omega) = \frac{e^2}{\varepsilon(\omega-\omega_c)^2}\exp\left\{-\left[\frac{e^2}{\varepsilon(\omega-\omega_c)} - r_0\right]^2/d^2\right\} \quad (14)$$

in which $\omega_c = E_0/\hbar$ is the electronic origin and ε is the dielectric constant of the medium. The identical spectrum would be obtained for a Coulomb potential at the origin and an initial state density shifted onto a shell at $r = r_0$. In the present, the scattering is into the oxide, on an effectively one-dimensional potential along z.

With the substitution of eq 14 on the LHS of eq 11, experimental spectra can be fitted, with effective screened charge $\alpha = e^2/\varepsilon$, initial state confinement, d, and Coulomb shell radius, r_0, as fitting parameters. We first fit the BL spectrum with its single resonance. Since in the progression the interference is between individual discrete resonances and a single background, the spectrum, $I(\omega)$, is given as

$$I(\omega) = \sum_j \mathscr{L}_j^*(\omega)\mathscr{L}_j(\omega) = \sum_{j=1}^{N}\left|\frac{\csc(\phi_j)e^{-i\phi_j}}{1-i\varepsilon_j} + i\frac{c(\omega)}{N}\right|^2 \quad (15)$$

where j identifies the individual members of the progression. The procedure yields a nearly perfect fit of the spectra, as in Figure 4. The identical background function $c(\omega)$ fits the spectra on the BL and SL. The most meaningful parameter extracted from the fit to the background is the steepness of the Coulomb potential defined by the local dielectric constant ε in eq 14. Perhaps fortuitous, $\varepsilon = 8.5$ is obtained, which is in

TABLE 1. Extracted Parameters from the Fano Line Shape Fit of the Progression in Electroluminescence Spectrum

	1	2	3	4	5	6	7
ϕ (rad)	2.904	2.686	3.022	3.084	3.061	3.026	2.894
ε_0 (eV)	1.427	1.530	1.578	1.612	1.658	1.670	1.739
γ (eV)	0.036	0.013	0.014	0.023	0.035	0.022	0.023

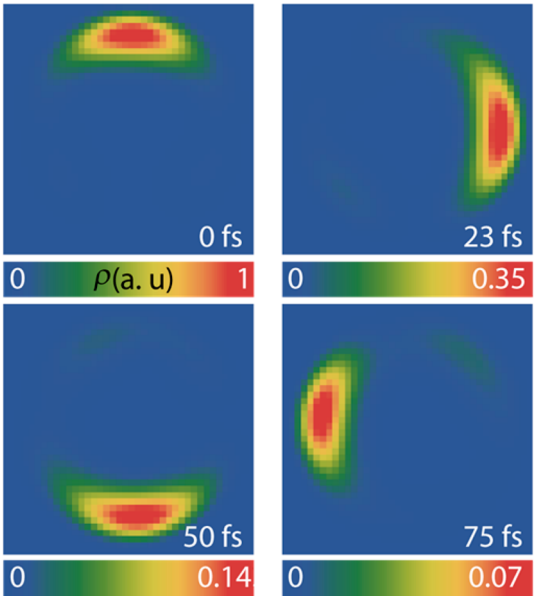

Figure 5. Time sequence of the electron density extracted from the Fano progression.

excellent agreement with the dielectric constant $\varepsilon = 9$ of Al_2O_3.[54] The extracted set of parameters, $\{\omega_i, \phi_i, \gamma_i\}$, which along with $c(t)$ define the time evolution of the system (eq 11) are collected in Table 1. Using the spatial wave functions (eq 3), the space−time-dependent electronic wave functions of the discrete states is defined:

$$\psi_l(r, \vartheta, t) = \psi_l(r, \vartheta)\csc(\phi)e^{-i\phi_l}e^{-(i\omega_l + \gamma_l/2)t} \quad (16)$$

The motion of the orbiting electron packet is obtained as the time-dependent density:

$$\rho(t) = \sum_{l,m} \psi_l(r, \vartheta, t)\psi_m^*(r, \vartheta, t) \quad (17)$$

Snapshots of this evolving density are shown in Figure 5. The EL spectroscopic measurements allow direct visualization of the electronic motion initiated by the sudden reduction of the $ZnEtio^-$ radical anion. The decay time of the wave function is 23 fs, which is in good agreement with the lifetime (35 fs) of the terminal state assigned from the d*I*/d*V* curve.

CONCLUSIONS

Spectroscopy within a single molecule offers a unique perspective into the inner workings of a molecule. Understanding the operating mechanism of the mixed electron−photon probe that allows submolecular spatial resolution is essential to extract the information content in such measurements. The assignment of molecular electroluminescence at the STM junction to radiative ionization explains the radiative rates required for the process to be observable, and a direct extension of this interpretation provides a rationale for STM-Raman with submolecular spatial resolution. The framework allows a unified interpretation of topography, d*I*/d*V* and EL spectra, and their spatial maps in the JT-active $ZnEtio^-$ radical anion. Electronic state assignments reduce to inspection of the symmetries in spatial maps, which can be recognized as the Franck−Condon maps of the electronic transitions. We have illustrated this by the complete electronic state assignment, including the identification of nonradiative curve crossings between electronic states in real space. Radiative ionization naturally explains the dispersive line shapes observed in EL, as the coupling between continuum and discrete shape resonances. Remarkably, the dispersive progressions can be used to recreate the time-dependent motion of the orbiting electron. The decay time of the reconstructed time-dependent electron density validates that the sharp resonance is the terminal state for the radiative transition. We show with complete generality that Fano progressions can be uniquely transformed to the time domain. To this end, we provided a general formulation of the Fano line shape that incorporates physically motivated backgrounds that can be used to fit spectra and to extract their underlying time domain dynamics. In effect, EL-STM is shown to allow spectroscopy with joint fs−Å resolution.

METHODS

The measurements are carried out in a low-temperature UHV STM, with base temperature and pressure of 5 K and 2×10^{-11} Torr, respectively. ZnEtio is sublimed on a 5 Å thick aluminum oxide layer grown on atomically flat NiAl(110), according to established procedures.[55] The instrument is equipped with a parabolic reflector that can be aligned *in situ* through a stack of three piezo stages (Attocube) for precise alignment of its focal point with the STM junction (Figure 1b). The system allows imaging of EL through a 0.3 m monochromator on the liquid nitrogen cooled charge-coupled device (CCD) plane. The parabolic reflector is aligned such that this EL reflector image is symmetric in the *xy*-plane and collimated along the *z*-axis. The APD and CCD are used to carry out total photon count imaging and spatially resolved spectral mapping, respectively.

Conflict of Interest: The authors declare no competing financial interest.

Acknowledgment. This research was made possible through the unique opportunities granted by the NSF Center for Chemical Innovation dedicated to Chemistry at the Space-Time Limit (CHE-082913). A.R. is grateful for his NSF graduate research fellowship (DGE-0808392). G. V. Nazin, Q. Huan, S. Yan, and W. Xing contributed to the construction of the optical STM under Prof. W. Ho's supervision. We have greatly benefitted from our discussions with K. Honkala and P. El-Khoury, who have carried out DFT calculations on the system.

REFERENCES AND NOTES

1. Qiu, X. H.; Nazin, G. V.; Ho, W. Vibrationally Resolved Fluorescence Excited with Submolecular Precision. *Science* **2003**, *299*, 542–546.
2. Chen, C.; Chu, P.; Bobisch, C. A.; Mills, D. L.; Ho, W. Viewing the Interior of a Single Molecule: Vibronically Resolved Photon Imaging at Submolecular Resolution. *Phys. Rev. Lett.* **2010**, *105*, 217402.
3. Zhang, R.; Zhang, Y.; Dong, Z. C.; Jiang, S.; Zhang, C.; Chen, L. G.; Zhang, L.; Liao, Y.; Aizpurua, J.; Luo, Y.; *et al.* Chemical Mapping of a Single Molecule by Plasmon-Enhanced Raman Scattering. *Nature* **2013**, *498*, 82–86.
4. Zhang, C.; Zhang, R.; Jiang, S.; Zhang, L.; Gao, H. Y.; Zhang, X. L.; Chen, L. G.; Liao, Y.; Dong, Z. C. Tip-Plasmon Mediated Molecular Electroluminescence on the Highly Oriented Pyrolytic Graphite Substrate. *Appl. Phys. Lett.* **2012**, *100*, 073111.
5. Dong, Z. C.; Zhang, X. L.; Gao, H. Y.; Luo, Y.; Zhang, C.; Chen, L. G.; Zhang, R.; Tao, X.; Zhang, Y.; Yang, J. L.; *et al.* Generation of Molecular Hot Electroluminescence by Resonant Nanocavity Plasmons. *Nat. Photonics* **2009**, *4*, 50–54.
6. Steidtner, J.; Pettinger, B. Tip-Enhanced Raman Spectroscopy and Microscopy on Single Dye Molecules with 15 nm Resolution. *Phys. Rev. Lett.* **2008**, *100*, 236101.
7. Sonntag, M. D.; Klingsporn, J. M.; Garibay, L. K.; Roberts, J. M.; Dieringer, J. A.; Seideman, T.; Scheidt, K. A.; Jensen, L.; Schatz, G. C.; Van Duyne, R. P. Single-Molecule Tip-Enhanced Raman Spectroscopy. *J. Phys. Chem. C* **2012**, *116*, 478–483.
8. Banik, M.; El-Khoury, P. Z.; Nag, A.; Rodriguez Perez, A.; Guarrottxena, N.; Bazan, G. C.; Apkarian, V. A. Surface-Enhanced Raman Trajectories on a Nano-Dumbbell: Transition from Field to Charge Transfer Plasmons as the Spheres Fuse. *ACS Nano* **2012**, *6*, 10343.
9. Buker, J.; Kirczenow, G. Understanding the Electroluminescence Emitted by Single Molecules in Scanning Tunneling Microscopy Experiments. *Phys. Rev. B* **2008**, *78*, 125107.
10. Seldenthuis, J. S.; van der Zant, H. S. J.; Ratner, M. A.; Thijssen, J. M. Electroluminescence Spectra in Weakly Coupled Single-Molecule Junctions. *Phys. Rev. B* **2010**, *81*, 205430.
11. Lee, J.; Perdue, S. M.; Rodriguez Perez, A.; El-Khoury, P. Z.; Honkala, K.; Apkarian, V. A. Orbiting Orbitals: Visualization of Vibronic Motion at a Conical Intersection. *J. Phys. Chem. A* **2013**, *117*, 11655–11664.
12. Coombs, J. H.; Gimzewski, J. K.; Reihl, B.; Sass, J. K.; Schlittler, R. R. Photon Emission Experiments with the Scanning Tunnelling Microscope. *J. Microsc.* **1988**, *152*, 325–336.
13. Hoffmann, G.; Kliewer, J.; Berndt, R. Luminescence from Metallic Quantum Wells in a Scanning Tunneling Microscope. *Phys. Rev. Lett.* **2001**, *87*, 176803.
14. Nilius, N.; Ernst, N.; Freund, H. Photon Emission Spectroscopy of Individual Oxide-Supported Silver Clusters in a Scanning Tunneling Microscope. *Phys. Rev. Lett.* **2000**, *84*, 3994–3997.
15. Dong, Z. C.; Guo, X. L.; Trifonov, A.; Dorozhkin, P.; Miki, K.; Kimura, K.; Yokoyama, S.; Mashiko, S. Vibrationally Resolved Fluorescence from Organic Molecules Near Metal Surfaces in a Scanning Tunneling Microscope. *Phys. Rev. Lett.* **2004**, *92*, 086801.
16. Ćavar, E.; Blüm, M.-C.; Pivetta, M.; Patthey, F.; Chergui, M.; Schneider, W.-D. Fluorescence and Phosphorescence from Individual C60 Molecules Excited by Local Electron Tunneling. *Phys. Rev. Lett.* **2005**, *95*, 196102.
17. Persson, B. N. J.; Baratoff, A. Theory of Photon Emission in Electron Tunneling to Metallic Particles. *Phys. Rev. Lett.* **1992**, *68*, 3224–3227.
18. Aizpurua, J.; Apell, S.; Berndt, R. Role of Tip Shape in Light Emission from the Scanning Tunneling Microscope. *Phys. Rev. B* **2000**, *62*, 2065–2073.
19. Chu, P.; Mills, D. L. Plasmonic Response of STM Tips. *Phys. Rev. B* **2011**, *84*, 045430.
20. Blanco, L.; García de Abajo, F. Spontaneous Light Emission in Complex Nanostructures. *Phys. Rev. B* **2004**, *69*, 205414.
21. Gouterman, M. Spectra of Porphyrins. *J. Mol. Spectrosc.* **1961**, *6*, 138–163.
22. Fano, U. Effects of Configuration Interaction on Intensities and Phase Shifts. *Phys. Rev.* **1961**, *124*, 1866–1878.
23. Fano, U. Sullo Spettro Di Assorbimento Dei Gas Nobili Presso Il Limite Dello Spettro D'arco. *Nuovo Cim.* **1935**, *12*, 154–161.
24. Bersuker, I. B.; Stavrov, S. S. Structure and Properties of Metalloporphyrins and Hemoproteins: The Vibronic Approach. *Coord. Chem. Rev.* **1988**, *88*, 1–68.
25. Private communication with Dr. K. Honkala.
26. Nazin, G. V.; Wu, S. W.; Ho, W. Tunneling Rates in Electron Transport through Double-Barrier Molecular Junctions in a Scanning Tunneling Microscope. *Proc. Natl. Acad. Sci. U.S.A.* **2005**, *102*, 8832–8837.
27. Datta, S. *Quantum Transport: Atom to Transistor*; Cambridge University Press: New York, 2005.
28. Buckman, S. J.; Clark, C. W. Atomic Negative-Ion Resonances. *Rev. Mod. Phys.* **1994**, *66*, 539–655.
29. Schulz, G. Resonances in Electron Impact on Diatomic Molecules. *Rev. Mod. Phys.* **1973**, *45*, 423–486.
30. Demuth, J.; Schmeisser, D.; Avouris, P. Resonance Scattering of Electrons from N_2, CO, O_2, and H_2 Adsorbed on a Silver Surface. *Phys. Rev. Lett.* **1981**, *47*, 1166–1169.
31. Nöckel, J. U.; Stone, A. D. Resonance Line Shapes in Quasi-One-Dimensional Scattering. *Phys. Rev. B* **1994**, *50*, 17415–17432.
32. Rau, A. R. P. Perspectives on the Fano Resonance Formula. *Phys. Scr.* **2004**, *69*, C10–C13.
33. Joe, Y. S.; Satanin, A. M.; Kim, C. S. Classical Analogy of Fano Resonances. *Phys. Scr.* **2006**, *74*, 259–266.
34. Schultz, M.; Nunner, T.; von Oppen, F. Berry-Phase Effects in Transport through Single Jahn–Teller Molecules. *Phys. Rev. B* **2008**, *77*, 075323.
35. Lee, H. J.; Lee, J.; Ho, W. Vibronic Transitions in Single Metalloporphyrins. *ChemPhysChem* **2005**, *6*, 971–975.
36. Schmid, M.; Shishkin, M.; Kresse, G.; Napetschnig, E.; Varga, P.; Kulawik, M.; Nilius, N.; Rust, H. P.; Freund, H. J. Oxygen-Deficient Line Defects in an Ultrathin Aluminum Oxide Film. *Phys. Rev. Lett.* **2006**, *97*, 046101.
37. Scheller, M. K; Compton, R. N.; Cederbaum, S. Gas-Phase Multiply Charged Anions. *Science* **1995**, *270*, 1160–1166.
38. Wang, L.-S.; Ding, C.-F.; Wang, X.-B.; Nicholas, J. B. Probing the Potential Barrier and Intramolecular Electrostatic Interactions in Free Doubly Charged Anions. *Phys. Rev. Lett.* **1998**, *81*, 2667–2670.
39. Li, Q.; Callaway, J. Exact Solutions for Two Interacting Particles in a One-Dimensional Ring with a Magnetic Flux. *Phys. Rev. B* **1991**, *43*, 3278–3283.
40. Child, M. S. Dynamical Jahn–Teller Effect in Molecules Possessing One Four-Fold Symmetry Axis. *Mol. Phys.* **1960**, *3*, 601–603.
41. Yoshizawa, K.; Nakayama, T.; Kamachi, T.; Kozlowski, P. M. Vibronic Interaction in Metalloporphyrin π-Anion Radicals. *J. Phys. Chem. A* **2007**, *111*, 852–857.
42. Bersuker, I. B. *The Jahn–Teller Effect*; Cambridge University Press: Cambridge, UK, 2006; pp 91–95.
43. Markiewicz, R. Chaos in a Jahn–Teller Molecule. *Phys. Rev. E* **2001**, *64*, 026216.
44. Loorits, V. Exact Solutions in Some Jahn–Teller and Pseudo-Jahn–Teller Systems. *J. Phys. C Solid State Phys.* **1983**, *16*, L711–L715.
45. Judd, B. R. Exact Solutions to a Class of Jahn–Teller Systems. *J. Phys. C Solid State Phys.* **1979**, *12*, 1685–1692.
46. Ballhausen, C. J. Jahn–Teller Configurational Instability in Square-Planar Complexes. *Theor. Chim. Acta* **1965**, *3*, 368–374.
47. Miliordos, E. Hückel *versus* Möbius Aromaticity: The Particle in a Cylinder *versus* a Möbius Strip. *Phys. Rev. A* **2010**, *82*, 062118.
48. Strauss, H. L. Pseudorotation: A Large Amplitude Molecular Motion. *Annu. Rev. Phys. Chem.* **1983**, *34*, 301–328.
49. Wu, S. W.; Ogawa, N.; Ho, W. Atomic-Scale Coupling of Photons to Single-Molecule Junctions. *Science* **2006**, *312*, 1362–1365.

50. Chen, C. J. *Introduction to Scanning Tunneling Microscopy (Monographs on the Physics and Chemistry of Materials)*, 2nd ed.; Oxford University Press: New York, 2008.
51. Tannor, D. J. *Introduction to Quantum Mechanics: A Time-Dependent Perspective*; University Science Books: Mill Valley, CA, 2007.
52. Branigan, E. T.; Halberstadt, N.; Apkarian, V. A. Solvation Dynamics through Raman Spectroscopy: Hydration of Br_2 and Br_3^-, and Solvation of Br_2 in Liquid Bromine. *J. Chem. Phys.* **2011**, *134*, 174503.
53. Heller, E. J. Quantum Corrections to Classical Photodissociation Models. *J. Chem. Phys.* **1978**, *68*, 2066–2075.
54. Gusev, E. P.; Copel, M.; Cartier, E. High Resolution Depth Profiling in Ultrathin Al_2O_3 Films on Si. *Appl. Phys. Lett.* **2000**, *76*, 176–178.
55. Jaeger, R. M.; Kuhlenbeck, H.; Freund, H.-J.; Wuttig, M.; Hoffmann, W.; Franchy, R.; Ibach, H. Formation of a Well-Ordered Aluminium Oxide Overlayer by Oxidation of NiAl(110). *Surf. Sci.* **1991**, *259*, 235–252.